Chemical Engineering Journal 420 (2021) 127637

Contents lists available at ScienceDirect

Chemical Engineering Journal

journal homepage: www.elsevier.com/locate/cej

Extremely stretchable and healable ionic conductive hydrogels fabricated by surface competitive coordination for human-motion detection

Yufeng Wang [a], Mike Tebyetekerwa [c], Ying Liu [a], Meng Wang [a], Jixin Zhu [d], Jingsan Xu [e], Chao Zhang [a,*], Tianxi Liu [a,b,*]

[a] State Key Laboratory for Modification of Chemical Fibers and Polymer Materials, College of Materials Science and Engineering, Innovation Center for Textile Science and Technology, Donghua University, Shanghai 201620, PR China
[b] Key Laboratory of Synthetic and Biological Colloids, Ministry of Education, School of Chemical and Material Engineering, Jiangnan University, Wuxi 214122, PR China
[c] Research School of Electrical, Energy and Materials Engineering, The Australian National University, Canberra 2601 ACT, Australia
[d] Shaanxi Institute of Flexible Electronics (SIFE), Northwestern Polytechnical University (NPU), 127 West Youyi Road, Xi'an 710072, PR China
[e] School of Chemistry, Physics and Mechanical Engineering, Queensland University of Technology, Brisbane, QLD 4001, Australia

ARTICLE INFO

Keywords:
Ionic conductive hydrogels
Self-buckled surface
Surface competitive coordination
Stretchability
Heat-accelerated self-healing
Wearable pressure sensor

ABSTRACT

The construction of a surface-wrinkled ionic conductive hydrogel with highly stretchable and healable properties for a skin-inspired pressure sensor is desirable yet challenging. Here, a stretching/competitively-coordinating/releasing (SCR) strategy is presented for preparing a self-buckled polyacrylamide/alginate hydrogel (SPAH). Due to its high stretchability, excellent ionic conductivity and programmable wrinkled surfaces, the SPAH can readily work as an ionic conductor in a healable skin-inspired pressure sensor with adaptability and multi-functionality, achieving a wide pressure response range (25–20000 Pa), high sensitivity towards strain (3.19 kPa^{-1}), low detection limit (<25 Pa) and excellent durability (>1400 cycles). As a proof-of-concept, a wearable SPAH pressure sensor can adequately monitor finger bending, knee flexion, speaking and breathing, showing high potentials in full-range and sophisticated motion monitoring across the applications involving human-machine interfaces, soft robotics, and artificial intelligence.

1. Introduction

Skin-inspired pressure sensors consist of mechanically flexible and pressure sensing networks capable of perceiving external stimuli and conducting tactile signals smoothly by mimicking a human skin, showing broad application prospects in emerging fields of wearable electronics [1–3], soft robotics [4–6], human–machine interfaces [7–9], and personal healthcare [10–12]. Ideal performances of skin-inspired pressure sensors are dictated by their mechanical flexibility, wide-range sensitivity and limit of detection (LOD) [13–20]. However, it is challenging to map all these qualities in one material especially for capacitive-type pressure sensors which present the merits of low power consumption, simple construction and high integration [21]. The ability to design complex surface microstructures (such as pyramids, cylinders, domes, *etc.*) on capacitive-type sensing materials can address the named issues [22–24]. This is ascribed to these structural designs presenting very low contact areas (without an external stimulus) and at the same time facilitating a massive change in contact area which can consequently command a significant capacitance response when an external stimulus is applied [25]. However, the capacitive-type sensing materials are currently confronted with poor mechanical flexibility and complexity in realizing their surface structures [3,26–28].

Ionic hydrogels with combined properties of high ionic conductivity, biocompatibility and tunable mechanical properties are highly attractive in new-emerging skin-inspired pressure sensors [29–31]. Ionic hydrogels rely on ion migrations to transmit electrical signals, overcoming the limitation of narrow reversible strain ranges of electronic conductors in capacitive skin-inspired pressure sensors [32,33]. Ionic hydrogels utilizing hydrogel matrices show similar compositions and mechanical properties to that of human skin [34–36]. However, ionic skin based on ionic hydrogels intrinsically suffers from poor mechanical performance, low sensitivity and insufficient cycling stability [37]. To improve these properties, the fabrication of a complex microstructure on ionic hydrogel surfaces can be realized by templating and 3D-printing

* Corresponding authors at: State Key Laboratory for Modification of Chemical Fibers and Polymer Materials, College of Materials Science and Engineering, Innovation Center for Textile Science and Technology, Donghua University, Shanghai 201620, PR China.
E-mail addresses: czhang@dhu.edu.cn (C. Zhang), txliu@fudan.edu.cn (T. Liu).

https://doi.org/10.1016/j.cej.2020.127637
Received 1 September 2020; Received in revised form 10 October 2020; Accepted 31 October 2020
Available online 5 November 2020

technologies [38], albeit rather with complicated approaches, which hinder the durability of the sensing devices with skyrocketing costs. Therefore, the realizations of ionic hydrogels with high mechanical strength, excellent sensitivity and reliable self-healing performance for the emerging ionic skin are extremely wanting, yet challenging [36].

Herein, a stretching/competitively-coordinating/releasing (SCR) strategy is presented for preparing a self-buckled polyacrylamide/alginate hydrogel (SPAH), during which a core-sheath film with a Ca^{2+} ion-coordinated PAH (Ca-PAH) core and Fe^{3+} ion-coordinated PAH (Fe-PAH) sheath is achieved by surface competitively coordinating of Ca-PAH homogeneity film with Fe^{3+} ions. The pre-stretching strain and sheath thickness are tailorable, facilitating hydrogel samples with precisely controlled surface wrinkles of tailored wavelengths and amplitudes. Owing to its extremely stretchable, ionic conductive and heat-accelerated self-healing properties, the SPAH exhibits an inspiring skin-inspired pressure sensing performance including a wide pressure range, short response time and high sensitivity with an extremely low LOD. The presented approach opens an avenue to fabricate surface-wrinkling ionic conductive hydrogels for ionic skin with adaptability and multifunctionality.

2. Results and discussion

Fig. 1a illustrates the preparation procedures of SPAH in a three-step SCR strategy. First, a Ca-PAH film with a semi-interpenetrating hydrogel network was prepared by in-situ polymerization of acrylamide (AAm) in a mixed solution of sodium alginate (Na-Alg) and Ca^{2+} ions. Among the Ca-PAH, PAAm chains were chemically crosslinked by N,N'-methylene bis(acrylamide) (MBAA), and Alg chains were physically crosslinked by Ca^{2+} ions. Second, the Ca-PAH film was pre-stretched at a specific strain and immersed into an aqueous solution of $Fe_2(SO_4)_3$, during which Fe^{3+} ions gradually infiltrated into the Ca-PAH film and competitively coordinated with the Alg chains due to the stronger coordination interaction of Fe^{3+} ions than that of Ca^{2+} ions. A core-sheath SPAH with a tailored thickness of Fe-PAH sheath was obtained by tailoring the soaking time. Third, the SPAH film was then obtained by releasing the external stress.

During the formation of SPAH, the Ca-PAH core recovered its original shape, whereas the Fe-PAH sheath that was already fixed in a stretching shape would form a self-buckled structure firmly attached to Ca-PAH core. Fig. 1b and 1c show the photographs of the Ca-PAH and SPAH, respectively. The SPAH film was light brown and translucent compared with the Ca-PAH due to the attachment of Fe^{3+} ions on the surface of the film. A tailored wrinkled structure was formed on the SPAH surface while Ca-PAH film showed a smooth surface, verified by top- and side-view scanning electron microscopy (SEM) images of Ca-PAH (Fig. 1d, e) and SPAH (Fig. 1f, g). Fig. S1 demonstrated that the as-fabricated wrinkling structure of SPAH was highly stable when aged for 3 days. Interestingly, the SCR strategy is general and easily extended to fabricating surface-wrinkling ionic hydrogels in complex shapes. For instances, the SPAH in shapes of cylindrical fiber, bent fiber and twisted

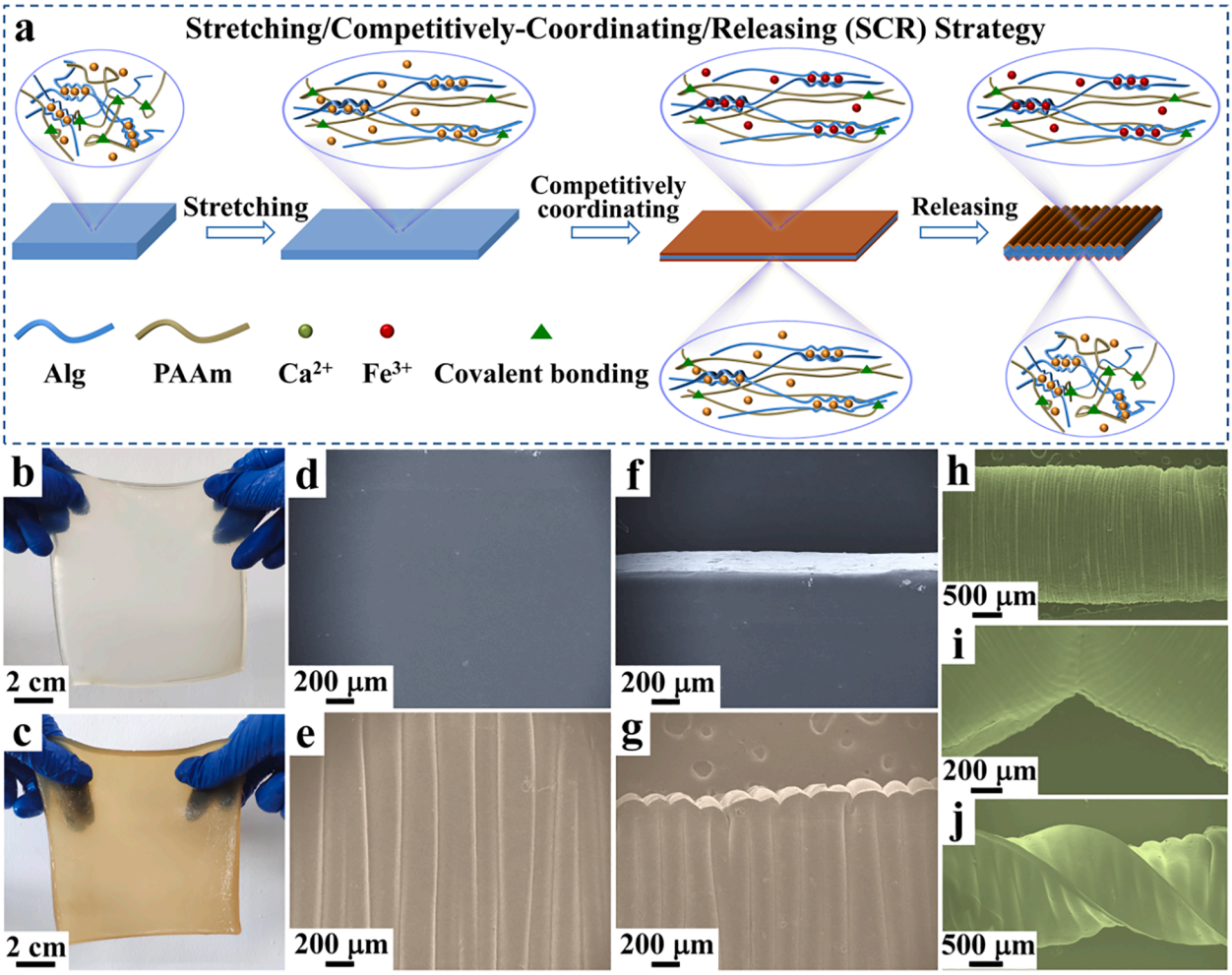

Fig. 1. a) Schematic illustration of the preparation procedures of SPAH. Photographs showing b) Ca-PAH and c) SPAH. Top-view SEM images of d) Ca-PAH and e) SPAH. Side-view SEM images of f) Ca-PAH and g) SPAH. Photographs of examples of SPAH in shapes of h) cylindrical fiber, i) bent fiber and j) twisted belt fabricated using the above SCR processes.

belt were successfully fabricated using the SCR strategy (Fig. 1h–j).

The deformation recovery property of the inner and outer layer among PAH core-sheath film is a critical factor for the formation of SPAH. The mechanical performance of the PAH with tailored Na-Alg/AAm ratios was investigated (Fig. S2). The tensile moduli and mechanical strengths of PAH increased with an increase of Na-Alg within the PAH, indicating that the existence of the rigid Alg network in PAH is conducive to the enhancement of gel rigidity. The metal-coordinated PAH samples (M−PAH) showed very different mechanical properties. Fig. S3 shows the photograph of Na-PAH coordinated with a variety of cations (e.g., Mn^{2+}, Zn^{2+}, Ca^{2+}, Al^{3+}, Fe^{3+}), respectively, and the chelation of these cations with Alg chains was confirmed by the Fourier transform infrared (FTIR) spectra (Fig. S4, summarized in Table S1). The infrared peaks corresponding to the symmetric and asymmetric stretching vibrations of carboxylic groups (s($-COO^-$)) blue- and red-shifted, respectively, upon the coordination of Alg with cations [39–41]. The Fe-PAH showed an elastic modulus and fracture strength of 276 and 758 kPa (Fig. S5), respectively. The Fe-PAH demonstrated more excellent mechanical properties than those of Mn-PAH, Zn-PAH, Ca-PAH and Al-PAH, due to Fe-PAH having a relatively high crosslinking density, confirmed by its lowest equilibrium swelling ratio (ESR) (Fig. S6) and largest storage modulus derived from the rheological measurements (Fig. S7) [42]. More importantly, when pre-stretched Ca-PAH was coordinated with trivalent cations for sufficient time, the internal stress almost disappeared when the external stress was released. In contrast, the internal stresses of pre-stretched Ca-PAH coordinated with divalent cations remained (Fig. S8). The difference in crosslinking intensity between different cations on PAH samples is key to the implementation of the SCR strategy. Furthermore, the M−PAH not only exhibited enhanced mechanical strengths but also showed heat-accelerated self-healing performance (Fig. S9). After heated at 70 °C for 2 h, the Ca-PAH (Fig. S9a) and Fe-PAH (Fig. S9b) achieved a healing efficiency (HE) of 38% and 49%, respectively. The high HE of Fe-PAH is ascribed to the dense bonding of Fe^{3+} ions to Alg chains.

Amplitude (A) and wavelength (λ) are two key parameters defining surface wrinkles of SPAH. Fig. 2a demonstrates a schematic illustration for the construction of SPAH with tailored surface wrinkles. The wrinkled surface of SPAH was tailored by varying pre-stretching strain and soaking time, respectively. The SPAH-0, SPAH-50, SPAH-100, SPAH-200, SPAH-300, SPAH-400 and SPAH-500 represent the Ca-PAH that was pre-stretched to a specific strain of 0, 50%, 100%, 200%, 300%, 400% and 500%, respectively, while keeping soaking time at 30 s. The 5-SPAH, 10-SPAH, 15-SPAH, 30-SPAH and 10000-SPAH represent the Ca-PAH which was soaked in Fe^{3+} ion solution at soaking time of 5, 10, 15, 30 and 10000 s, respectively, while keeping pre-stretching strain at 300% (Table S2).

The pre-stretching strain and soaking time are respectively customized for the initial strain (ε_{pre}) and shell thickness (h_s) of SPAH. Fig. S10a-f show SEM images of designed wrinkled surface among the SPAH-50, SPAH-100, SPAH-200, SPAH-300, SPAH-400 and SPAH-500, respectively. The SPAH-50 exhibited a slightly wrinkled surface, and this trend became evident with the gradually increased pre-stretching strain, indicating that the pre-stretching strain is an essential factor in generating the wrinkles. The top-view SEM image of SPAH further illustrated this trend (Fig. S11a–f), and the wavelengths of wrinkles did not change significantly with an increased pre-stretching strain. The relationship between the wrinkles and pre-stretching strain was analyzed by the wrinkle generation equations as follows [43,44]:

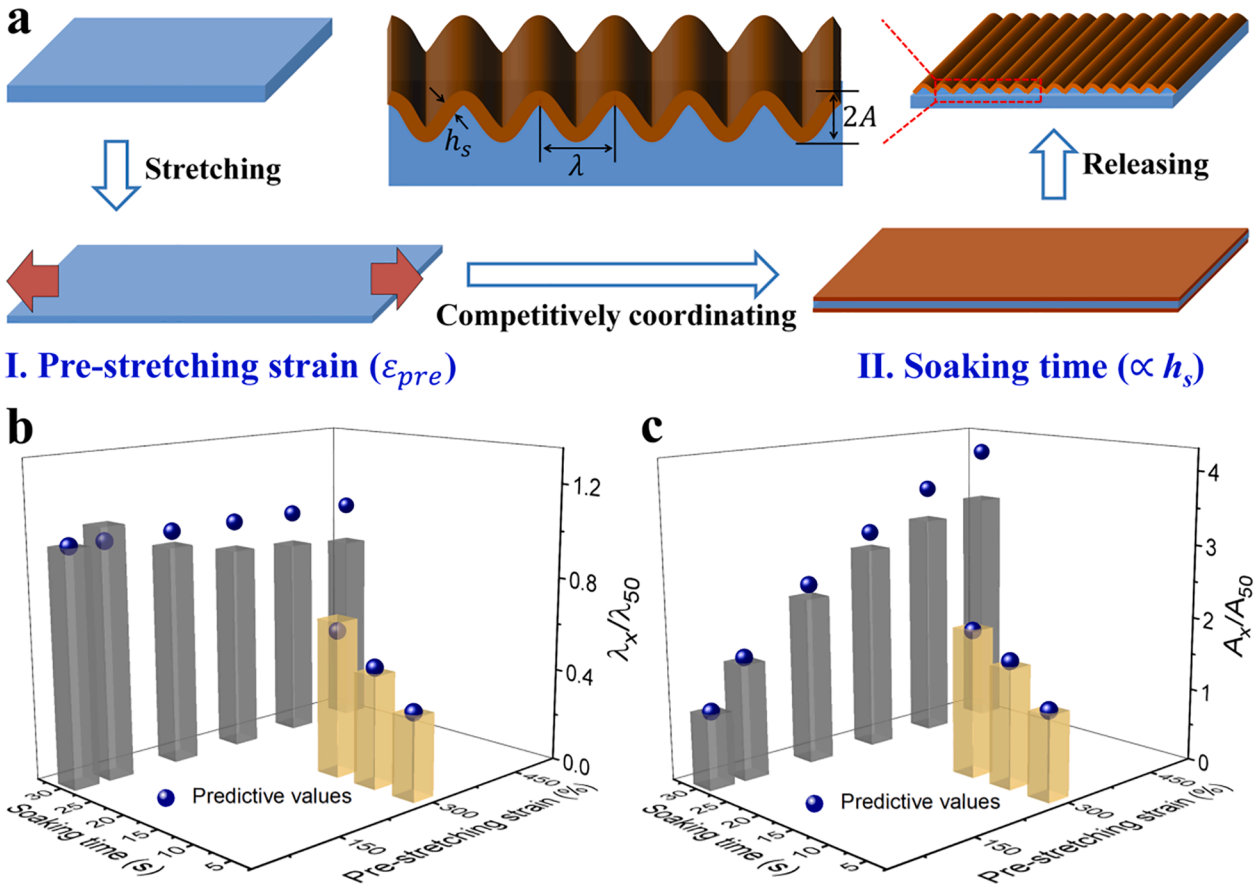

Fig. 2. Regulation of surface wrinkling wavelength (λ) and amplitude ($2A$) of SPAH. a) Schematic illustration of SPAH with surface wrinkles of regulated wavelength and amplitude. Regulation of b) wavelength and c) amplitude of SPAH by tailoring soaking time and pre-stretching strain.

$$\sigma_c = 0.25\overline{E_s} \times (\frac{3\overline{E_c}}{\overline{E_s}})^{2/3} \quad (1)$$

$$\varepsilon_c = 0.25 \times (\frac{3\overline{E_c}}{\overline{E_s}})^{2/3} \quad (2)$$

$$\lambda = 2\pi h_s \times (\frac{\overline{E_c}}{3\overline{E_s}})^{1/3} \quad (3)$$

$$A \propto h_s \sqrt{\frac{\varepsilon_{pre}}{\varepsilon_c} - 1} \quad (4)$$

$$\overline{E} = \frac{E}{1-\nu^2} \quad (5)$$

where σ_c and ε_c are the critical stress and strain for wrinkles, respectively, ε_{pre} is the pre-stretched strain, $\overline{E_c}$ and$\overline{E_s}$ are the plane strain modulus for core and shell, respectively, h_s is the thickness of shell, and ν is Poisson's ratio. To correlate the soaking time with shell thickness, we used the following equation: $\frac{t_1}{t_2} = \frac{h_{s1}^2}{h_{s2}^2}$ [45]. In particular, the ε_c was calculated to be 0.2 by Eq. (1), which was slightly less than the practical strain applied to hydrogels. Eq. (3) showed that the wavelength was dependent on pre-stretching strain, suggesting proper consistency with experimental results. The relationship between the shell thickness and wrinkle structure was also discussed. Fig. S12a–d show the SEM images of a 300% pre-stretched Ca-PAH at soaking time of 5, 10, 15 and 30 s, respectively. The vibration wavelength exhibited a significant change with soaking time. With an increase in soaking time, the vibration wavelength also increased, due to the h_s coordinated by Fe^{3+} ions increased with soaking time, and Eq. (3) showed that h_s was proportional to λ. Fig. S13 shows the EDS mappings of SPAH-30, demonstrating that Fe^{3+} ions were uniformly distributed within the whole SPAH-30 when the SPAH-30 was stored in humidity box at 25 °C for 24 h. The result showed that even if the hydrogel was only immersed in Fe^{3+} ion solution for very short time to get a SPAH, the excess Fe^{3+} ions in the shell would gradually diffuse to the whole hydrogel but the wrinkled surface structure was well maintained. However, when pre-stretched hydrogel was immersed in Fe^{3+} ion solution for 10000 s, the surface of hydrogel showed no longer wrinkles (Fig. S14). This was because the whole hydrogel network was immobilized by the secondary coordination crosslinking of Fe^{3+}, and there was no internal stress in the inner and outer layers of hydrogels. The experimental results and theoretical

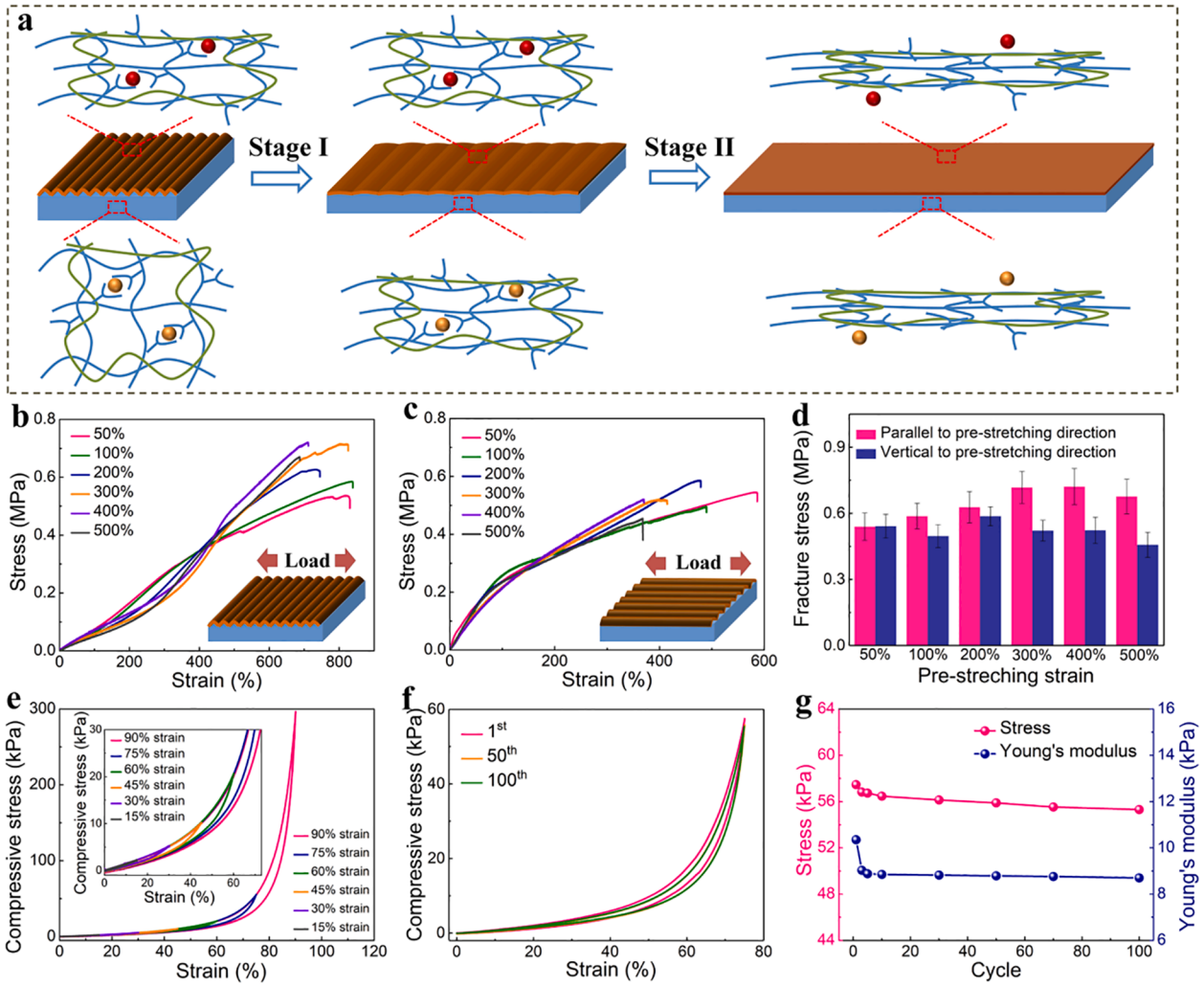

Fig. 3. Mechanical performance of SPAH. a) Schematic illustration of tensile processes of SPAH at different strain stages (Stage I: lower than pre-stretching strain; Stage II: larger than pre-stretching strain). Tensile stress–strain curves of SPAH prepared at different pre-stretching strains in the direction b) parallel to and c) perpendicular to pre-stretching. Insets of b) and c) showing the schematic of direction for tensile tests. d) Fracture strength of SPAH prepared at different pre-stretching strains in the direction parallel to and perpendicular to pre-stretching. e) Compressive stress/strain curves of SPAH under different strains. Inset of e) showing the enlarged view. f) Compressive fatigue test with 75% compressive strain for 100 cycles. g) Young's modulus and maximum stress as a function of compressive cycles.

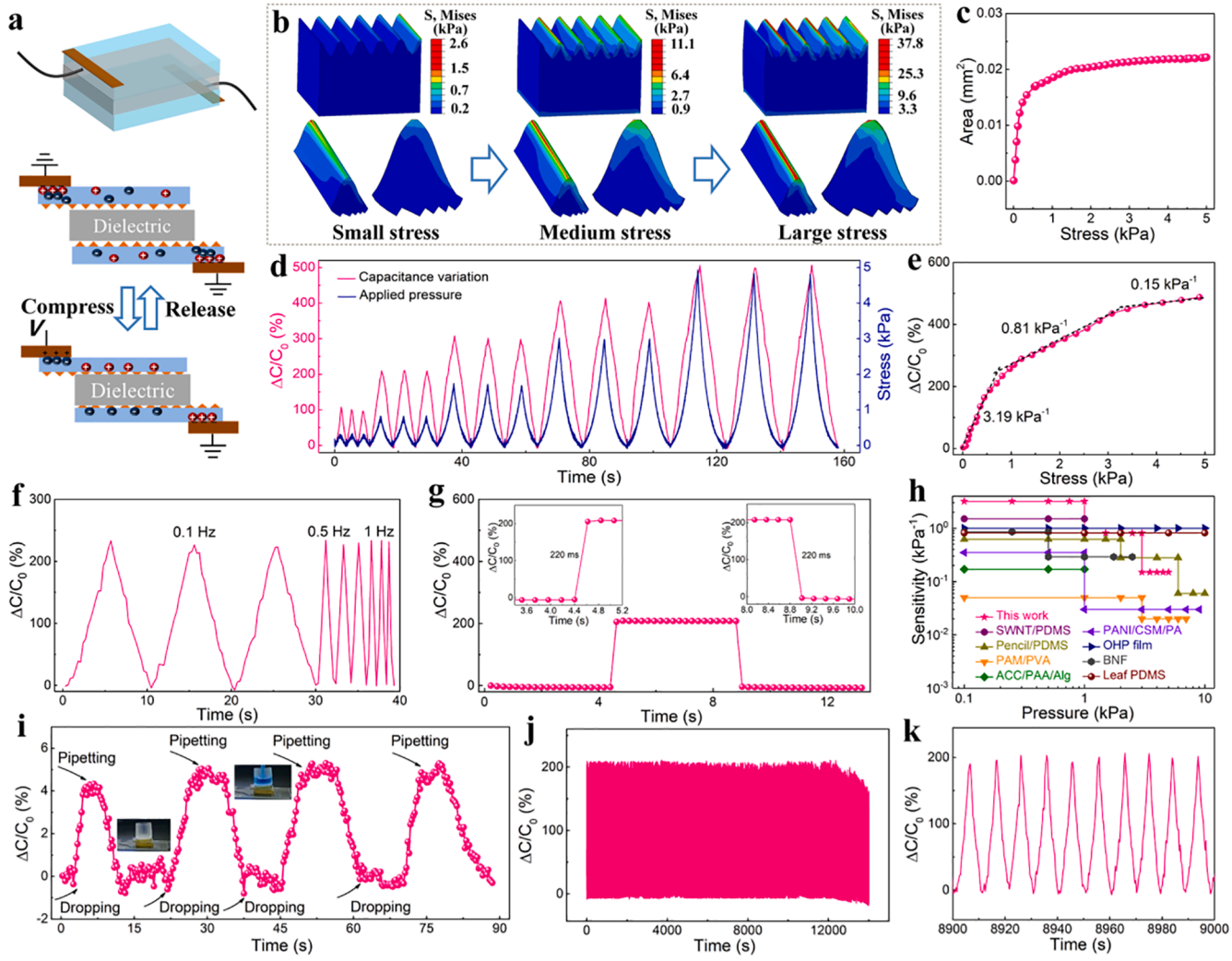

Fig. 4. Capacitive pressure sensing performance of SPAH. a) Schematic diagram of as-assembled capacitive pressure sensor. b) Stress distributions of SPAH under 0.5, 1, 5 kPa by the FEA method. c) Contact areas between SPAH and dielectric layer as a function of applied stress. d) Normalized capacitance variation and applied stress under cyclic compressing/releasing process between 0.3 and 5 kPa. e) Normalized capacitance variation at different compressive stresses. f) Normalized capacitance variation at different loading frequency at 1 kPa. g) Capacitance response to instantaneous stress. Insets of g) showing the response and recovery time, respectively. h) Comparison of SPAH and previously reported capacitive pressure sensors. i) Real-time response of SPAH capacitive pressure sensor detecting water dropping and pipetting. j) Working stability of SPAH capacitive pressure sensor for 14000 s under 1 kPa. k) Recorded normalized capacitance variation from 8900 to 9000 s.

predictions of the λ and A of the SPAH were calculated in Fig. 2b, c and summarized in Tables S3 and S4. It was found that the experimental results agreed well with theoretical predictions at the small pre-stretching strain, and the experimental results slightly deviated from theoretical predictions at the large pre-stretching strain. The deviation was attributed to the internal extrusion of SPAH during large pre-stretching strains, which caused the formation of wrinkles to be hindered.

The SCR strategy achieved a unique wrinkling interface of a soft Ca-PAH and stiff Fe-PAH segments among the SPAH. As a result, the SPAH exhibited an unusual combination of mechanical properties with high mechanical strength and toughness through the incorporation of wrinkling interface. To evaluate the impact of the integrated soft-stiff wrinkling interface that was formed via the SCR on the mechanical properties of as-fabricated SPAH, the tensile stress–strain performance of SPAH in the vertical and parallel directions to pre-stretched axis were measured. Fig. 3a shows the microstructural evolution of SPAH under tensile deformations in the direction parallel to pre-stretched axis. The SPAH displayed a weak loading in stage I, especially for the SPAH prepared with a sizeable pre-stretching strain (Fig. 3b), attributed to fracture of the coordinated network along the tensile direction during pre-stretching. Meanwhile, the wrinkle amplitude of SPAH gradually decreased with increased tensile strain (Fig. S15a, under 150% strain). The stiff Fe-PAH sheath layer among the SPAH only deformed through the unfolding of wrinkles at this stage, and the hydrogel network of Fe-PAH layer was not substantially stretched, resulting in a response to weak loading during the tensile. In stage II, under the tensile strain larger than that of pre-stretching strain, the surface wrinkling structure of SPAH disappeared completely (Fig. S15b, under 300% strain), and the stress increased rapidly with increased strain. The ions used for crosslinking the hydrogel network were dragged out to release huge energy dissipations to achieve a high toughness of SPAH. However, in the vertical direction, no weak

loading was observed in the initial tensile region for SPAH (Fig. 3c). Besides, the tensile strength and fracture strain of SPAH in the parallel direction were higher than those in the vertical direction (Fig. 3d). The high fracture strain of SPAH in the parallel direction was attributed to the formation of wrinkling surface structures. In the parallel direction, the wrinkling structure deformed along with the external force. In contrast, in the vertical direction, the wrinkling structure confronted with the external force, resulting in the fracture of hydrogel networks. The SCR strategy, therefore, reduces the damage of external force to the hydrogel structure, resulting in primarily enhanced tensile strength and mechanical ductility of SPAH in the pre-stretched direction. The SPAH exhibited a negligible hysteresis when the SPAH was undergoing a loading/unloading tensile test at various tensile strains (Fig. S16), indicating its excellent tensile recovery performance. In a successive cyclic tensile fatigue test with 100 cycles at a 100% strain, the SPAH showed a slightly decreased maximum stress with small plastic deformation, indicating its excellent fatigue resistance (Fig. S17).

Fig. S18a shows the tensile stress–strain performance of SPAH-50 along the pre-stretched axis that was prepared at different soaking time. The tensile strength of Ca-PAH was 346 kPa, while the tensile strength of SPAH-50 with soaking time of 30 and 10000 s increased by ~ 55% and ~ 110%, respectively. The enhancements in tensile strength with increased soaking time were also observed in the SPAH-100, SPAH-200, SPAH-300, SPAH-400 and SPAH-500 (Fig. S18b–f). Also, the increase in tensile strength became more evident with the increased pre-stretching strain. The enhanced mechanical properties of SPAH were explained as follows: (1) The crosslinking density of Fe-PAH increased with the increase of soaking time; (2) The crosslinking intensity of Fe-PAH was much stronger than that of Ca-PAH; (3) The pre-stretching and secondary coordinating enabled the hydrogel with an oriented pore structure along the pre-stretching direction, and the anisotropic structure was beneficial to enhance the mechanical strength and modulus.

The SPAH obtained by the SCR strategy was subjected to freeze-drying to observe its pore structures (Fig. S19a). Fig. S19b–h exhibit the SEM images of freeze-dried SPAH samples with a pre-stretching

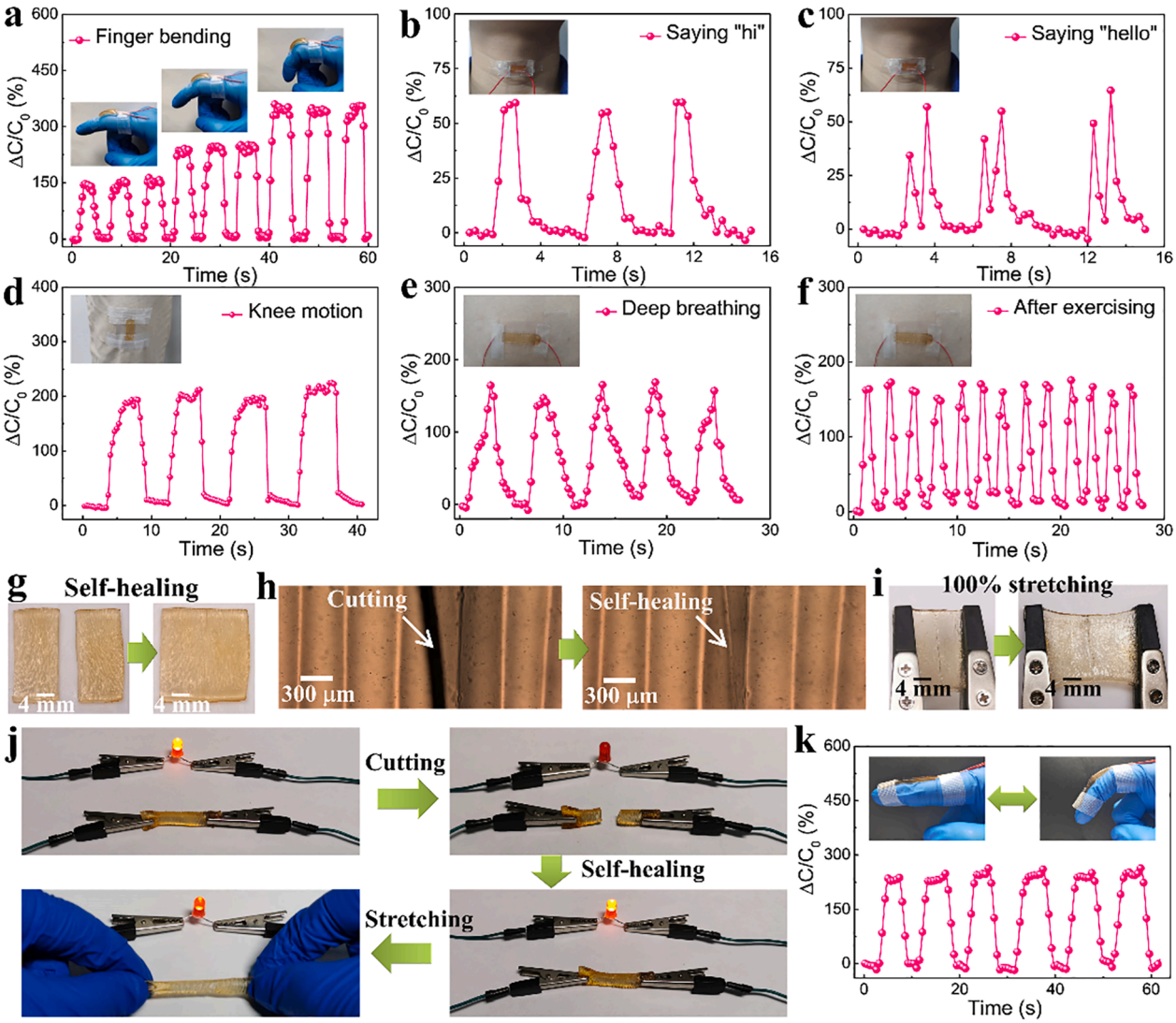

Fig. 5. Wearable and self-healing properties of SPAH capacitive pressure sensor. a) Real-time capacitance signals when a finger was bent at different degrees. b, c) Real-time capacitance signals when the wearer said "hi" and "hello". d) Real-time capacitance signals when a knee was bent cyclically. e) Real-time capacitance signals when the wearer was deep breathing. f) Real-time capacitance signals when the wearer was breathing after exercising. g) Photographs showing self-healing behaviors of two pieces of SPAH merging into a whole. h) Optical microscope images of fractured and healed SPAH. i) Photographs showing a healable SPAH under stretching at a 100% strain. j) Photographs showing the SPAH connected into a circuit lightening up an LED upon self-healing and stretching. k) Real-time capacitance signals for SPAH capacitive sensor when a finger was bent cyclically upon self-healing.

strain of 0, 50%, 100%, 200%, 300%, 400% and 500%, respectively. The soaking time is set at 10000 s to ensure the full coordination crosslinking for the formation of SPAH. The hydrogel sample without any pre-stretching exhibited a randomly oriented 3D porous structure due to the ice templating during freeze-drying (Fig. S19b). However, the pre-stretched hydrogel showed an aligned and ordered structure along the pre-stretching direction. The orientated pore structures were pronounced, especially under a large pre-stretching strain (Fig. S19c–h). During the tensile, the randomly oriented pore structure absorbed excess energy through deformation, endowing hydrogel samples with high toughness [46].

The SPAH not only exhibited excellent stretchable properties, but also showed an outstanding compressive elasticity with high shape-recovery ability. The SPAH sample exhibited a fully shape-recovery performance with almost no plastic deformation even at a considerable compressive strain of 90% (Fig. 3e). Excellent elastic performance was observed in Ca-PAH and Fe-PAH samples (Fig. S20a, b). The SPAH possessed an elastic modulus of 10.5 kPa, which was higher than that of Ca-PAH (9.7 kPa), but lower than that of Fe-PAH (31.3 kPa). Considerable enhancement in the elastic modulus of Fe-PAH was ascribed to its denser crosslinking density than that of Ca-PAH and SPAH. In a successive cyclic compression test with 100 cycles at a 75% strain, the stress and elastic modulus of SPAH and Ca-PAH decreased slightly in the first three cycles. Still, they remained always in the same compression cycles (Figs. 3f, g and S20c), demonstrating that the SPAH and Ca-PAH had excellent fatigue resistance and provided a guarantee for stable sensing performance [47]. The SEM image indicated that the wrinkling structure of SPAH exhibited no obvious damages after 100 compressive cycles (Fig. S21), indicating the excellent structural stability of SPAH. However, significant stress and modulus losses were observed in the Fe-PAH during the continuous loading–unloading cycles (Fig. S20d), attributing to the destruction of the crosslinking network of Fe-PAH during successive loading–unloading cycles [48].

The pressure-sensing performance of SPAH samples was evaluated and measured in a typical capacitive pressure sensor device, according to Eq. (6) by determining the capacitance in a parallel plate capacitor:

$$C = \frac{\varepsilon S}{4\pi k d} \tag{6}$$

where C is the capacitance, ε is the dielectric constant, k is the electrostatic constant, S is the effective area of the electrode, and d is the distance between two electrodes. Typically, a decreased distance between the two electrodes or an expanding area of the electrode leads to increased capacitance. The capacitive pressure sensor was constructed by integrating two pieces of SPAH samples with a dielectric layer (Fig. 4a). When subjected to an external force, the effective area of the electrode changed, resulting in the change of capacitance of the sensor. Due to the unique wrinkling surface of SPAH, the SPAH pressure sensor produced large area changes when subjected to external pressure, thereby generating a huge capacitance response. The stress distributions and changes of contact areas under light and heavy forces (0.5, 1 and 5 kPa) were simulated by the finite element analysis (FEA) method, demonstrating the microstructure evolution of high-sensitivity SPAH pressure sensor under small to large pressures. In a low-stress range, the local stress mainly concentrated on the top of the wrinkles (Fig. 4b), and the applied small stress produced large changes in contact areas. However, in the media and large stress regions (Fig. 4b), a relatively lower stress-area response than that in the low-stress region was demonstrated. Consequently, the SPAH ionic skin showed high sensitivity in the low-stress region, but relatively low sensitivity in the large stress region (Fig. 4c). The real-time responses of the pressure sensor with the loading–unloading pressure ranges (0.3–5 and 0.3–20 kPa, respectively) were tested (Figs. 4d and S22). The SPAH capacitive ionic sensor well repeated the responses for multiple times without significant changes in the capacitance. The pressure sensitivity of the SPAH capacitive sensor was defined by Eq. (7):

$$S = \frac{\delta(\Delta C/C_0)}{\delta P} \tag{7}$$

where ΔC is the relative change of capacitance, C_0 is the initial capacitance, and P is the applied pressure. The SPAH capacitive sensor exhibited three distinct linear capacitance segments depending on varied compressive pressures (Fig. 4e). The skin-like sensor showed a high sensitivity of 3.19 kPa^{-1} at a low-pressure range (<0.5 kPa) in the first segment. A sensitivity of 0.81 kPa^{-1} was achieved at a pressure range from 0.5 to 3 kPa in the second segment. In the third segment (3–5 kPa), the sensor exhibited a relatively low sensitivity of 0.15 kPa^{-1}. The unique wrinkling surface of SPAH contributed to non-linear marginal variations under the varied applied pressures. The wrinkling structure of the SPAH was first compressed and gradually squashed into a flat morphology with an increased pressure, causing an enormous change in the contact areas. When the pressure further increased, however, the increased active area depended on the deformation of SPAH under the pressure. For comparison, a sensor with wrinkle-free Ca-PAH exhibited a stable capacitive response but with a low sensitivity of 0.13 kPa^{-1} (Fig. S23a, b), clearly proving that the design of surface winkling ionic hydrogels dramatically improved the sensitivity of as-fabricated capacitive pressure sensors.

The SPAH capacitive sensor was moreover measured at various loading speeds, to simulate the actual sensing processes of a sensor in dynamic consecutive pressure detection. Fig. 4f showed that a continuous, stable and highly repeatable capacitive response upon 1 kPa with a pressure frequency ranging from 0.1 to 1 Hz was achieved, indicating that the ionic skin sensor was not affected by frequency of the applied pressure. The response time of the SPAH capacitive sensor was investigated upon 1 kPa with an instantaneous pressure (Fig. 4g), indicating that the capacitive sensor possessed a short response and recovery time of < 220 ms. Not only that, but the sensor was also subjected to consecutively dropping/pipetting water of 0.6 g (<25 Pa) for multiple cycles, to investigate the LOD of the sensor. The SPAH capacitive sensor showed a higher sensitivity than those of capacitive sensors based on ionic conductive hydrogels and elastomers (Figs. 4h and S24), compared with previously reported results of pressure sensors [47,49–55]. The ionic skin sensor showed the ability of detecting the gradually injected water with an upward trend in the capacitance (Fig. 4i, Movie S1). The capacitance of the sensor restored to its initial value when the water was gradually retrieved. The low LOD of the capacitive sensor increased derived from its unique wrinkling structure of SPAH. Furthermore, the relative capacitance variation of the SPAH capacitive sensor displayed high durability under the 1 kPa pressure loading (Fig. 4j). The magnified view (Fig. 4k) clearly illustrated that the capacitance signals from loading/unloading cycles at 8900 to 9000 s kept a similar waveform and amplitude. The SPAH was also assembled into a tensile strain sensor. Fig. S25 showed that the capacitance-strain curve of the SPAH capacitive sensor was highly reversible when the sensor was undergoing loading–unloading cycles within a strain range of 0–100%.

Movie S1.

A wearable SPAH capacitive sensor was assembled to detect the biomedical signals and clinical diagnosis, *i.e.*, finger motions, speaking and breathing. Fig. 5a and Movie S2 exhibited the as-assembled SPAH capacitive sensor for monitoring finger bending processes with different bending angles (30°, 60° and 90°). The signal waves of amplitudes were related to bending degrees of the finger. The device deformed drastically leading to an enhancement in the signal wave when increasing the degree of finger bending. For capturing the vibrations of the vocal cords during the speech, the ionic skin sensor was attached to the throat. Various words, such as "hi" and "hello", were detected with characteristic signal patterns by the device (Fig. 5b, c). Each word was repeated many times without apparent changes in the signal wave. Fig. 5d showed that the SPAH capacitive sensor was also capable of detecting knee movements. Besides, when the sensor was attached to the abdomen, the heaving caused by the breath was detected in real-time. As a result, the breath rates of the measured human under normal condition and after exercising were calculated as ~ 12 and 29 times min^{-1} (Fig. 5e, f, Movie S3), respectively.

Movie S2.

Movie S3.

The SPAH sample showed an excellent self-healing property. When two fractured SPAH samples were in contact with each other, they recombined into one whole and repaired the crack after heating at 70 °C for 2 h (Fig. 5g). No noticeable cracking was observed in the two parts of hydrogel samples during the deformation after the heat-accelerated self-healing. Fig. 5h showed that the cutmarks on the SPAH almost disappeared after heating the sample, indicating that the incision of SPAH upon damage was repaired. As a result, the healable SPAH showed the ability to be stretched at a 100% strain and recovered its initial shape repeatedly (Fig. 5i). A piece of SPAH was bounded onto conductive clips to construct a closed-loop circuit (Fig. 5j). Due to its high ionic conductivity and desirable self-healing performance, a light-emitting diode (LED) was lightened up when the SPAH sample was heated and healed to form a complete whole after cutting into two pieces. Upon self-healing, the SPAH sample still showed the ability to lighten up the LED as a stretchable conductive wire, further verifying its outstanding self-healing and stretchable performance. The EIS curves showed that a similar semicircle to initial SPAH was observed when SPAH was cut and healed at 70 °C for 2 h, indicating the ionic conductivity of SPAH was recovered upon healing (Fig. S26a). The ionic conductivity of SPAH was as high as 0.087 S m^{-1}. For comparison, the semicircle of healed SPAH was larger than initial SPAH when it was cut and healed at room temperature for 2 h, indicating that the heating accelerated the movement of the gel network and therefore improved the healing performance (Fig. S26b). Besides, the reliability of the SPAH ionic skin sensor in the case of damages was further evaluated. Fractured parts of SPAH were assembled in an ionic capacitive sensor. Upon thermal stimulation for self-healing, the healed device responded well to bending and straightening motions of fingers, while exhibiting excellent stability during repeated damage/healing processes (Fig. 5k).

3. Conclusion

In summary, an ionic conductive hydrogel with precise tailoring of wrinkling amplitudes and wavelengths was achieved by surface competitive coordination. The as-fabricated SPAH demonstrated unique features of high stretchability, tailored wrinkled surfaces and heat-accelerated healable properties, which was further used as a healable ionic conductor for assembling a skin-inspired capacitive pressure sensor. The SPAH capacitive pressure sensor delivered a high sensitivity (3.19 kPa^{-1}), low LOD (25 Pa), excellent durability (>1400 cycles). As a proof-of-concept, the wearable SPAH pressure sensor demonstrated excellent monitoring of human motions (e.g., finger bending, speaking, and breathing). Importantly, the SPAH pressure sensor showed a remarkable heat-accelerated self-healing ability, largely improving its safety and service life. The developed SCR strategy opens a new avenue to fabricate ionic conductive hydrogels with programmable wrinkled surfaces, and the wearable SPAH pressure sensors also render them great prospects in new-emerging adaptable and multi-functional ionic skins.

4. Materials and methods

4.1. Preparation of M−PAH

The Ca-PAH was prepared by in-situ polymerization of AAM in a mixed aqueous solution of Na-Alg and $CaSO_4·2H_2O$. Typically, 0.75 g Na-Alg and 6.00 g AAm were dissolved into 40 mL of DI water. The MBAA (0.06 wt% of AAm), APS (4 wt% of AAm) and $CaSO_4·2H_2O$ (1 wt % of Na-Alg) were then added in turn under stirring. Upon vacuum degassing to remove gas bubbles, the mixed solution was casted into a poly(tetra fluoroethylene) (PTFE) mold (50 × 5 × 2 mm^3), kept at 60 °C for 4 h, and aged at 25 °C for 24 h. For comparison, the Fe-PAH, Mn-PAH, Zn-PAH and Al-PAH represent the PAH samples prepared by replacing the $CaSO_4·2H_2O$ with $Fe_2(SO_4)_3·H_2O$, $MnSO_4·4H_2O$, $ZnSO_4·7H_2O$, $Al_2(SO_4)_3·18H_2O$, respectively, while keeping other conditions same as the Ca-PAH. The PAAm, PAH-1, PAH-2 and PAH-3 represent the PAH samples prepared by varying the initial Na-Alg at 0, 0.375, 0.750 and 1.125 g, respectively, while keeping other conditions same as the Ca-PAH yet without the addition of $CaSO_4·2H_2O$.

4.2. Preparation of Ca/Fe-PAH

The Ca/Fe-PAH was prepared in an SCR process using a Ca-PAH film as precursor. Typically, the Ca-PAH film was pre-stretched at a specific strain of 50%, 100%, 200%, 300%, 400% and 500%, respectively. The Ca-PAH was then immersed into a 0.1 M $Fe_2(SO_4)_3$ solution while maintaining the pre-strain, and the soaking time was kept at 5, 10, 15, 30 and 10000 s, respectively. The Ca/Fe-PAH was then obtained after releasing the external stress.

4.3. Measurements of capacitive pressure sensor

Capacitive pressure sensing performance of hydrogel samples was measured on an LCR meter (TH2832) at a sweeping frequency of 1 kHz and AC voltage of 1 V. The capacitive pressure sensor was assembled with two hydrogel samples (20 × 15 × 2 mm^3) sandwiched with a polyethylene dielectric layer (thickness: 0.1 mm). Two outermost pieces of copper foils as current collectors were used to connect testing wires. The as-assembled capacitive pressure sensor was wholly packaged by an elastomer tape (3 M VHB 4905) to prevent water evaporation.

4.4. Computational models and methods

Numerical simulations were performed using the Abaqus. The inner and outer layers of SPAH films were partitioned, and the respective material properties such as elasticity modulus, Poisson's ratio, and material size were assigned at each section. The model was composed of C3D8R and C3D6 element types using 34,700 elements and 38,073 nodes. The load was applied to the top of SPAH films, and the applied load gradually increased from 0 to 5 kPa.

Declaration of Competing Interest

The authors declare that they have no known competing financial interests or personal relationships that could have appeared to influence the work reported in this paper.

Acknowledgements

We are grateful for the financial support from the National Natural Science Foundation of China (21875033), the Shanghai Rising-Star Program (18QA1400200), Ministry of Education of the People's Republic of China (6141A02033233) and the Shanghai Scientific and Technological Innovation Project (18JC1410600).

Appendix A. Supplementary data

Supplementary data to this article can be found online at https://doi.org/10.1016/j.cej.2020.127637.

References

[1] K. Senthil Kumar, P.Y. Chen, H. Ren, A review of printable flexible and stretchable tactile sensors, Research 2019 (2019) 3018568.
[2] L. Li, Y. Zhang, H. Lu, Y. Wang, J. Xu, J. Zhu, C. Zhang, T. Liu, Cryopolymerization enables anisotropic polyaniline hybrid hydrogels with superelasticity and highly deformation-tolerant electrochemical energy storage, Nat. Commun. 11 (2020) 62.
[3] A. Chortos, J. Liu, Z. Bao, Pursuing prosthetic electronic skin, Nat. Mater. 15 (2016) 937–950.
[4] D. Chen, Q. Pei, Electronic muscles and skins: a review of soft sensors and actuators, Chem. Rev. 117 (2017) 11239–11268.
[5] Y. Ding, J. Zhang, L. Chang, X. Zhang, H. Liu, L. Jiang, Preparation of high-performance ionogels with excellent transparency, good mechanical strength, and high conductivity, Adv. Mater. 29 (2017) 1704253.

[6] G.-H. Yu, Q. Han, L.-T. Qu, Graphene fibers: advancing applications in sensor, energy storage and conversion, Chin. J. Polym. Sci. 37 (2019) 535–547.
[7] H. Yuk, S. Lin, C. Ma, M. Takaffoli, N.X. Fang, X. Zhao, Hydraulic hydrogel actuators and robots optically and sonically camouflaged in water, Nat. Commun. 8 (2017) 14230.
[8] S. Choi, Y. Choi, J. Kim, Anisotropic hybrid hydrogels with superior mechanical properties reminiscent of tendons or ligaments, Adv. Funct. Mater. 29 (2019) 1904342.
[9] J.-Y. Sun, C. Keplinger, G.M. Whitesides, Z. Suo, Ionic skin, Adv. Mater. 26 (2014) 7608–7614.
[10] Y. Lu, X. Qu, W. Zhao, Y. Ren, W. Si, W. Wang, Q. Wang, W. Huang, X. Dong, Highly stretchable, elastic, and sensitive MXene-based hydrogel for flexible strain and pressure sensors, Research 2020 (2020) 1–13.
[11] Z. Li, L. Ye, J. Shen, K. Xie, Y. Li, Strain-gauge sensoring composite films with self-restoring water-repellent properties for monitoring human movements, Compos. Commun. 7 (2018) 23–29.
[12] W. Zhang, C. Xu, C. Ma, G. Li, Y. Wang, K. Zhang, F. Li, C. Liu, H.M. Cheng, Y. Du, N. Tang, W. Ren, Nitrogen-superdoped 3D graphene networks for high-performance supercapacitors, Adv. Mater. 29 (2017) 1701677.
[13] Y.u. Pang, K. Zhang, Z. Yang, S. Jiang, Z. Ju, Y. Li, X. Wang, D. Wang, M. Jian, Y. Zhang, R. Liang, H.e. Tian, Y.i. Yang, T.-L. Ren, Epidermis microstructure inspired graphene pressure sensor with random distributed spinosum for high sensitivity and large linearity, ACS Nano 12 (2018) 2346–2354.
[14] X. Liu, H. Yuk, S. Lin, G.A. Parada, T.C. Tang, E. Tham, C. de la Fuente-Nunez, T. K. Lu, X. Zhao, 3D printing of living responsive materials and devices, Adv. Mater. 30 (2018) 1704821.
[15] Q. Rong, W. Lei, L. Chen, Y. Yin, J. Zhou, M. Liu, Anti-freezing, conductive self-healing organohydrogels with stable strain-sensitivity at subzero temperatures, Angew. Chem. Int. Ed. 56 (2017) 14159–14163.
[16] R. Wang, N. Jiang, J. Su, Q. Yin, Y. Zhang, Z. Liu, H. Lin, F.A. Moura, N. Yuan, S.J. A.F.M. Roth, A bi-sheath fiber sensor for giant tensile and torsional displacements, Adv. Funct. Mater. 27 (2017) 1702134.
[17] C. Feng, J. Zhang, Y. He, C. Zhong, W. Hu, L. Liu, Y. Deng, Sub-3 nm Co 3 O 4 nanofilms with enhanced supercapacitor properties, ACS Nano 9 (2015) 1730–1739.
[18] F. Chen, D. Zhou, J. Wang, T. Li, X. Zhou, T. Gan, S. Handschuh-Wang, X. Zhou, Rational fabrication of anti-freezing, non-drying tough organohydrogels by one-pot solvent displacement, Angew. Chem. Int. Ed. 57 (2018) 6568–6571.
[19] S. Jun, S.O. Kim, H.-J. Lee, C.J. Han, C.-J. Lee, Y.-T. Yu, C.-R. Lee, B.-K. Ju, Y. Kim, J.-W. Kim, Transparent, pressure-sensitive, and healable e-skin from a UV-cured polymer comprising dynamic urea bonds, J. Mater. Chem. A 7 (2019) 3101–3111.
[20] M. Tang, R. Zhang, J. Fang, S. Li, Y.-X. Xu, G. Huang, Ductile composites with strain hardening behavior constructing highly sensitive electronic sensor, Compos. Commun. 15 (2019) 20-24.
[21] M. Jian, K. Xia, Q. Wang, Z. Yin, H. Wang, C. Wang, H. Xie, M. Zhang, Y. Zhang, Flexible and highly sensitive pressure sensors based on bionic hierarchical structures, Adv. Funct. Mater. 27 (2017) 1606066.
[22] C.-L. Choong, M.-B. Shim, B.-S. Lee, S. Jeon, D.-S. Ko, T.-H. Kang, J. Bae, S.H. Lee, K.-E. Byun, J. Im, Y.J. Jeong, C.E. Park, J.-J. Park, U.-I. Chung, Highly stretchable resistive pressure sensors using a conductive elastomeric composite on a micropyramid array, Adv. Mater. 26 (2014) 3451–3458.
[23] Y. Park, J. Shim, S. Jeong, G.R. Yi, H. Chae, J.W. Bae, S.O. Kim, C. Pang, Microtopography-guided conductive patterns of liquid-driven graphene nanoplatelet networks for stretchable and skin-conformal sensor array, Adv. Mater. 29 (2017) 1606453.
[24] Z. Qiu, Y. Wan, W. Zhou, J. Yang, J. Yang, J. Huang, J. Zhang, Q. Liu, S. Huang, N. Bai, Z. Wu, W. Hong, H. Wang, C.F. Guo, Ionic skin with biomimetic dielectric layer templated from calathea zebrine leaf, Adv. Funct. Mater. 28 (2018) 1802343.
[25] W. Lei, S. Qi, Q. Rong, J. Huang, Y. Xu, R. Fang, K. Liu, L. Jiang, M. Liu, Diffusion-freezing-induced microphase separation for constructing large-area multiscale structures on hydrogel surfaces, Adv. Mater. 31 (2019) 1808217.
[26] M.L. Hammock, A. Chortos, B.C. Tee, J.B. Tok, Z. Bao, 25th anniversary article: The evolution of electronic skin (e-skin): a brief history, design considerations, and recent progress, Adv. Mater. 25 (2013) 5997–6038.
[27] Y. Liu, M. Pharr, G.A. Salvatore, Lab-on-skin: a review of flexible and stretchable electronics for wearable health monitoring, ACS Nano 11 (2017) 9614–9635.
[28] S.C.B. Mannsfeld, B.-K. Tee, R.M. Stoltenberg, C.-H. Chen, S. Barman, B.V.O. Muir, A.N. Sokolov, C. Reese, Z. Bao, Highly sensitive flexible pressure sensors with microstructured rubber dielectric layers, Nature Mater 9 (2010) 859–864.
[29] C. Yang, Z. Suo, Hydrogel ionotronics, Nat. Rev. Mater. 3 (2018) 125–142.
[30] Y. Gao, L. Shi, S. Lu, T. Zhu, X. Da, Y. Li, H. Bu, G. Gao, S. Ding, Highly stretchable organogel ionic conductors with extreme-temperature tolerance, Chem. Mater. 31 (2019) 3257–3264.
[31] Y. Zhou, C. Wan, Y. Yang, H. Yang, S. Wang, Z. Dai, K. Ji, H. Jiang, X. Chen, Y. Long, Highly stretchable, elastic, and ionic conductive hydrogel for artificial soft electronics, Adv. Funct. Mater. 29 (2019) 1806220.
[32] Y. Wu, D. Wang, I. Willner, Y. Tian, L. Jiang, Smart DNA hydrogel integrated nanochannels with high ion flux and adjustable selective ionic transport, Angew. Chem. Int. Ed. 57 (2018) 7790–7794.
[33] P. Lin, T. Zhang, X. Wang, B. Yu, F. Zhou, Freezing molecular orientation under stretch for high mechanical strength but anisotropic hydrogels, Small 12 (2016) 4386–4392.
[34] K.Y. Lee, D.J. Mooney, Alginate: properties and biomedical applications, Progr. Polym. Sci. 37 (2012) 106–126.
[35] L. Li, L. Pan, Z. Ma, K. Yan, W. Cheng, Y. Shi, G. Yu, All inkjet-printed amperometric multiplexed biosensors based on nanostructured conductive hydrogel electrodes, Nano Lett. 18 (2018) 3322–3327.
[36] L. Han, K. Liu, M. Wang, K. Wang, L. Fang, H. Chen, J. Zhou, X. Lu, Mussel-inspired adhesive and conductive hydrogel with long-lasting moisture and extreme temperature tolerance, Adv. Funct. Mater. 28 (2018) 1704195.
[37] W. Wang, Y. Zhang, W. Liu, Bioinspired fabrication of high strength hydrogels from non-covalent interactions, Prog. Polym. Sci. 71 (2017) 1–25.
[38] S.A. Rub Pakkath, S.S. Chetty, P. Selvarasu, A. Vadivel Murugan, Y. Kumar, L. Periyasamy, M. Santhakumar, S.R. Sadras, K. Santhakumar, Transition metal ion (Mn2+, Fe2+, Co2+, and Ni2+)-doped carbon dots synthesized via microwave-assisted pyrolysis: a potential nanoprobe for magneto-fluorescent dual-modality bioimaging, ACS Biomater. Sci. Eng. 4 (2018) 2582–2596.
[39] J. Luo, F. Kong, X. Ma, Role of aspartic acid in the synthesis of spherical vaterite by the Ca(OH)2–CO2 reaction, Cryst. Growth Des. 16 (2016) 728–736.
[40] H. Guo, J. Zhou, Q. Li, Y. Li, W. Zong, J. Zhu, J. Xu, C. Zhang, T. Liu, Emerging dual-channel transition-metal-oxide quasiaerogels by self-embedded templating, Adv. Funct. Mater. 30 (2020) 2000024.
[41] H. Guo, Q. Feng, K. Xu, J. Xu, J. Zhu, C. Zhang, T. Liu, Self-templated conversion of metallogel into heterostructured TMP@carbon quasiaerogels boosting bifunctional electrocatalysis, Adv. Funct. Mater. 29 (2019) 1903660.
[42] J. Cai, D. Ye, Y. Wu, L. Fan, H. Yu, Injectable alginate fibrous hydrogel with a three-dimensional network structure fabricated by microfluidic spinning, Compos. Commun. 15 (2019) 1–5.
[43] X. Chen, J.W. Hutchinson, Herringbone buckling patterns of compressed thin films on compliant substrates, J. Appl. Mech. 71 (2004) 597–603.
[44] S. Cai, D. Breid, A.J. Crosby, Z. Suo, J.W. Hutchinson, Periodic patterns and energy states of buckled films on compliant substrates, J. Mech. Phys. Solids 59 (2011) 1094–1114.
[45] C. Yang, M. Wang, H. Haider, J. Yang, J.-Y. Sun, Y. Chen, J. Zhou, Z. Suo, Strengthening alginate/polyacrylamide hydrogels using various multivalent cations, ACS Appl. Mater. Interf. 5 (2013) 10418–10422.
[46] J. Zou, S. Wu, J. Chen, X. Lei, Q. Li, H. Yu, S. Tang, D. Ye, Highly efficient and environmentally friendly fabrication of robust, programmable, and biocompatible anisotropic, all-cellulose, wrinkle-patterned hydrogels for cell alignment, Adv. Mater. 31 (2019) 1904762.
[47] L. Li, K. Wang, Z. Huang, C. Zhang, T. Liu, Highly ordered graphene architectures by duplicating melamine sponges as a three-dimensional deformation-tolerant electrode, Nano Res. 9 (2016) 2938–2949.
[48] L. Li, L. Xu, W. Ding, H. Lu, C. Zhang, T. Liu, Molecular-engineered hybrid carbon nanofillers for thermoplastic polyurethane nanocomposites with high mechanical strength and toughness, Compos. Part B 177 (2019), 107381.
[49] S. Park, H. Kim, M. Vosgueritchian, S. Cheon, H. Kim, J.H. Koo, T.R. Kim, S. Lee, G. Schwartz, H. Chang, Z. Bao, Stretchable energy-harvesting tactile electronic skin capable of differentiating multiple mechanical stimuli modes, Adv. Mater. 26 (2014) 7324–7332.
[50] K. Lee, J. Lee, G. Kim, Y. Kim, S. Kang, S. Cho, S. Kim, J.K. Kim, W. Lee, D.E. Kim, S. Kang, D.E. Kim, T. Lee, W. Shim, Rough-surface-enabled capacitive pressure sensors with 3D touch capability, Small 13 (2017) 1700368.
[51] J. Duan, X. Liang, J. Guo, K. Zhu, L. Zhang, Ultra-stretchable and force-sensitive hydrogels reinforced with chitosan microspheres embedded in polymer networks, Adv. Mater. 28 (2016) 8037–8044.
[52] Z. Lei, Q. Wang, S. Sun, W. Zhu, P. Wu, A bioinspired mineral hydrogel as a self-healable, mechanically adaptable ionic skin for highly sensitive pressure sensing, Adv. Mater. 29 (2017) 1700321.
[53] G. Ge, Y. Zhang, J. Shao, W. Wang, W. Si, W. Huang, X. Dong, Stretchable, transparent, and self-patterned hydrogel-based pressure sensor for human motions detection, Adv. Funct. Mater. 28 (2018) 1802576.
[54] R.Y. Tay, H. Li, J. Lin, H. Wang, J.S.K. Lim, S. Chen, W.L. Leong, S.H. Tsang, E.H. T. Teo, Lightweight, superelastic boron nitride/polydimethylsiloxane foam as air dielectric substitute for multifunctional capacitive sensor applications, Adv. Funct. Mater. 30 (2020) 1909604.
[55] H. Kim, G. Kim, T. Kim, S. Lee, D. Kang, M.S. Hwang, Y. Chae, S. Kang, H. Lee, H. G. Park, W. Shim, Transparent, flexible, conformal capacitive pressure sensors with nanoparticles, Small 14 (2018) 1870032.